J Neuropathol Exp Neurol
Vol. 72, No. 5
May 2013
pp. 386–395

ORIGINAL ARTICLE

OPEN

Synaptic Changes in the Dentate Gyrus of APP/PS1 Transgenic Mice Revealed by Electron Microscopy

Lidia Alonso-Nanclares, PhD, Paula Merino-Serrais, PhD, Santiago Gonzalez, PhD, and Javier DeFelipe, PhD

Abstract

Numerous studies have reported widespread synaptic dysfunction or loss in early stages of both Alzheimer disease (AD) patients and animal models; it is widely accepted that synapse loss is the major structural correlate of cognitive dysfunction. Elucidation of the changes that may affect synapses is crucial for understanding the pathogenic mechanisms underlying AD, but ultrastructural preservation of human postmortem brain tissue is often poor, and classical methods for quantification of synapses have significant technical limitations. We previously observed changes in dendritic spines in plaque-free regions of the neuropil of the dentate gyrus of double-transgenic APP/PS1 (amyloid precursor protein/presenilin 1) model mice by light microscopy. Here, we used electron microscopy to examine possible synaptic alterations in this region. We used standard stereologic techniques to determine numbers of synapses per volume. We were able to reconstruct and analyze thousands of synapses and their 3-dimensional characteristics using a focused ion beam/scanning electron microscope and 3-dimensional reconstruction software (EspINA), which performs semiautomated segmentation of synapses. Our results show that both numbers of synapses per volume and synaptic morphology are affected in plaque-free regions of APP/PS1 mice. Therefore, changes in the number and morphology of synapses seem to be widespread alterations in this animal model.

Key Words: 3-D reconstruction, Alzheimer disease, Focused ion beam, Scanning electron microscopy, Segmentation, Synapse, Quantification.

Instituto Cajal (CSIC) (LA-N, PM-S, JD); Laboratorio Cajal de Circuitos Corticales, Centro de Tecnología Biomédica, Universidad Politécnica de Madrid, Campus Montegancedo s/n (LA-N, PM-S, JD); Centro de Investigación Biomédica en Red sobre Enfermedades Neurodegenerativas (CIBERNED) (LA-N, PM-S, JD); and Laboratorio de Minerí a de Datos y Simulación (MIDAS), Centro de Tecnología Biomédica, Universidad Politécnica de Madrid, Campus Montegancedo s/n (SG), Madrid, Spain.

Send correspondence and reprint requests to: Lidia Alonso-Nanclares, PhD, Instituto Cajal (CSIC), Avda. Doctor Arce, 37, Madrid, 28002 Spain; E-mail: aidil@cajal.csic.es

This work was supported by grants from CIBERNED (CB06/05/0066), Fundación CIEN, and the the Spanish Ministry of Economy and Competitiveness (SAF2009-09394, BFU2012-34963, and the Cajal Blue Brain Project, Spanish partner of the Blue Brain Project initiative from EPFL).

Supplemental digital content is available for this article. Direct URL citations appear in the printed text and are provided in the HTML and PDF versions of this article on the journal's Web site (www.jneuropath.com).

INTRODUCTION

The major neuropathologic hallmarks of Alzheimer disease (AD) are plaques of extracellular fibrillar β-amyloid (Aβ) peptide, neurofibrillary tangles of aggregated hyperphosphorylated tau in neurons, and elevated levels of soluble Aβ oligomers. Alzheimer disease neuropathologic changes may appear decades before the clinical manifestations are evident (1). In a recent review on the correlation of Aβ plaques and neurofibrillary tangles with cognitive impairment, the authors concluded that, although Aβ plaques may play a key role in AD pathogenesis, the severity of cognitive impairment correlates best with the burden of neocortical neurofibrillary tangles (2). Other studies emphasize alterations at the synaptic level, suggesting that synapse loss is the major morphologic correlate of cognitive impairment (3–10).

The vast majority of synapses in the cerebral cortex are glutamatergic excitatory synapses (asymmetric synapses), and the main targets of these synapses are the dendritic spines (for simplicity, ''spines'') of spiny neurons (pyramidal neurons, spiny stellate cells, and granule cells of the dentate gyrus [DG]). There is a general consensus that dendritic spines are critical in memory, learning, and cognition. In this respect, the loss of dendritic spines has been reported in AD and in several AD mouse models (10). Because a key symptom in the early stages of AD is loss of declarative memory and the anatomic substrate that supports this kind of memory involves the neural circuits of the medial temporal lobe (particularly the hippocampal formation and adjacent cortex [11]), numerous laboratories have focused on these circuits. In this regard, the DG is one of the preferred structures for analysis in AD not only because of its involvement in the formation of new memories but also because it is one of the few brain structures showing significant neurogenesis in the adult mammalian brain. Moreover, impairment of this adult neurogenesis has been reported in AD patients (12).

In a previous study performed in our laboratory, focusing on the density and the 3-dimensional (3-D) analysis of spines from injected granular neurons in the DG with a fluorescent dye in double-transgenic amyloid precursor protein/presenilin 1 (APP/PS1) mice, we found that dendrites that passed through a plaque lost spines, whereas dendrites that were in contact with a plaque gained spines (13). Dendrites located in plaque-free areas showed a spine density similar to those of age-matched littermates that lacked the transgene (TG-) and served as controls. However, we found that there was a decreased frequency of large spines in plaque-free regions—a decrease of 38% in

the prevalence of spines whose head volume was more than 0.1 μm^3. Because plaques occupy a volume less than 4% of the DG molecular layer under our experimental conditions, we proposed that the widespread changes in plaque-free regions, corresponding to more than 95% of the neuropil, may have a more important influence on the cognitive deficits observed in these mice (10, 14).

In the present study, we investigated possible alterations at the synaptic level in the Aβ plaque-free regions from these APP/PS1 mice. More specifically, we analyzed synapses on the outer molecular layer of the DG in APP/PS1 mice and compared them with TG- mice. Several techniques were used to achieve our aims. First, quantitative analysis of the synaptic density per volume was performed using stereologic methods based on conventional transmission electron microscopy (TEM) samples (15). In addition, we used a new dual-beam electron microscope (EM), which combines a focused ion beam (FIB) column and a scanning electron microscope (SEM). We also used 3-D reconstruction software (EspINA) that performs semiautomated segmentation of synapses in a 3-D sample of tissue (16). Our results show that both the number of synapses per volume and the synaptic morphology are affected in the plaque-free regions of APP/PS1 mice.

MATERIALS AND METHODS

Tissue Preparation

The mouse line used for this study (APP/PS1, n = 5, aged 12–14 months) expressed Mo/Hu APP695swe construct in conjunction with the exon-9-deleted variant of human presenilin 1 (PS1-dE9) (17). Control mice were age-matched littermates without the transgene (TG-, n = 5, aged 12–14 months). To avoid possible effects of sex in the study, only male mice were used.

Mice were anesthetized with pentobarbital (0.04 mg/kg) and transcardially perfused with 20 mL of 0.1 mol/L phosphate buffer (PB) followed by 100 mL of 4% paraformaldehyde (0.1 mol/L, pH 7.4) made in the same buffer. The brains were removed from the skull and postfixed in the same solution for 24 hours. Coronal sections (50–150 μm) were cut with a vibratome. These sections were used for either light or EM analysis. All animals were handled in accordance with the guidelines for animal research set out in the European Community Directive 86/609/EEC, and all the procedures were approved by the local ethics committee of the Spanish National Research Council (CSIC).

Immunocytochemistry

Amyloid plaques were stained with an anti-human Aβ antibody. Free-floating sections (50 μm) were pretreated with 55% formic acid (Sigma-Aldrich, St. Louis, MO) and washed with PB. Sections were incubated for 2 hours in blocking solution: PB with 0.25% Triton X, 3% normal horse serum (Vector Laboratories Inc., Burlingame, CA). The sections were then incubated overnight at 4°C with a mouse anti-human Aβ antibody (1:50, clone 6F/3D; Dako, Glostrup, Denmark).

On the next day, the sections were rinsed and incubated for 2 hours with a biotinylated horse anti-mouse antibody (1:200; Vector Laboratories Inc.). The sections were then incubated for 1 hour in an avidin-biotin peroxidase complex (Vectastain ABC Elite PK6100; Vector Laboratories Inc.). Finally, the staining was visualized with the chromogen 3,3′-diaminobenzidine tetrahydrochloride (Sigma-Aldrich). After staining, the sections were dehydrated, cleared with xylene, and coverslipped. Slices were then counterstained with toluidine blue (Fig. 1A).

To generate the figures, images were captured with a digital camera (Olympus DP70) attached to an Olympus light microscope (Olympus, Ballerup, Denmark); Adobe Photoshop CS4 Extended 11.0.2 software (Adobe Systems, San Jose, CA) was used to produce the figure plates.

Electron Microscopy

Sections for EM were postfixed for 1 hour in 2% glutaraldehyde in PB, treated in 1% osmium tetroxide, dehydrated, and flat-embedded in Araldite resin. Plastic-embedded sections were studied by correlative light and EM, as previously described (18). Briefly, sections were photographed under the light microscope and then serially cut into semithin (2-μm-thick) sections with a Leica ultramicrotome (EM UC6; Leica Microsystems, Wetzlar, Germany). The semithin sections were stained with 1% toluidine blue in 1% borax, examined under the light microscope, and photographed to locate the area of interest (Fig. 1B). Selected semithin sections were resectioned into serial ultrathin sections with a silver-gray interference color, corresponding to a thickness of approximately 60 to 70 nm (19). The ultrathin sections were collected on formvar-coated, single-slot grids stained with uranyl acetate and lead citrate and examined using a JEOL TEM (JEM-1011; JEOL Ltd., Tokyo, Japan).

Selected regions of the neuropil on the surface of the tissue block were chosen for 3-D analysis. The 3-D study of the brain samples was carried out using an FIB/SEM (Crossbeam Neon40 energy-selective backscattered electron detector; Carl Zeiss NTS GmbH, Oberkochen, Germany).

Estimation of Synaptic Density by TEM

To estimate the synaptic density, photographs were taken randomly using a JEOL transmission EM with a digitalizing image system (SC1000 ORIUS, 11 megapixel; Gatan, Pleasanton, CA). Synapses were quantified in the neuropil (i.e. avoiding the neuronal and glial somata and blood vessels) (15). To obtain an adequate sample size, at least 30 micrographs were obtained per region and case at a magnification of 30,000× (20, 21). The 2 major morphologic types of cortical synapses were clearly identified in the cortical tissue analyzed (Fig. 2), that is, Gray's type I and type II synapses (22), which correspond to those denominated asymmetric and symmetric by Colonnier (23–25). Asymmetric synapses have a prominent postsynaptic density, whereas symmetric synapses have a thin postsynaptic density. The synapses in which the synaptic cleft and associated membrane densities could not be clearly visualized (because of the oblique plane of section) were considered to be uncharacterized synapses (15).

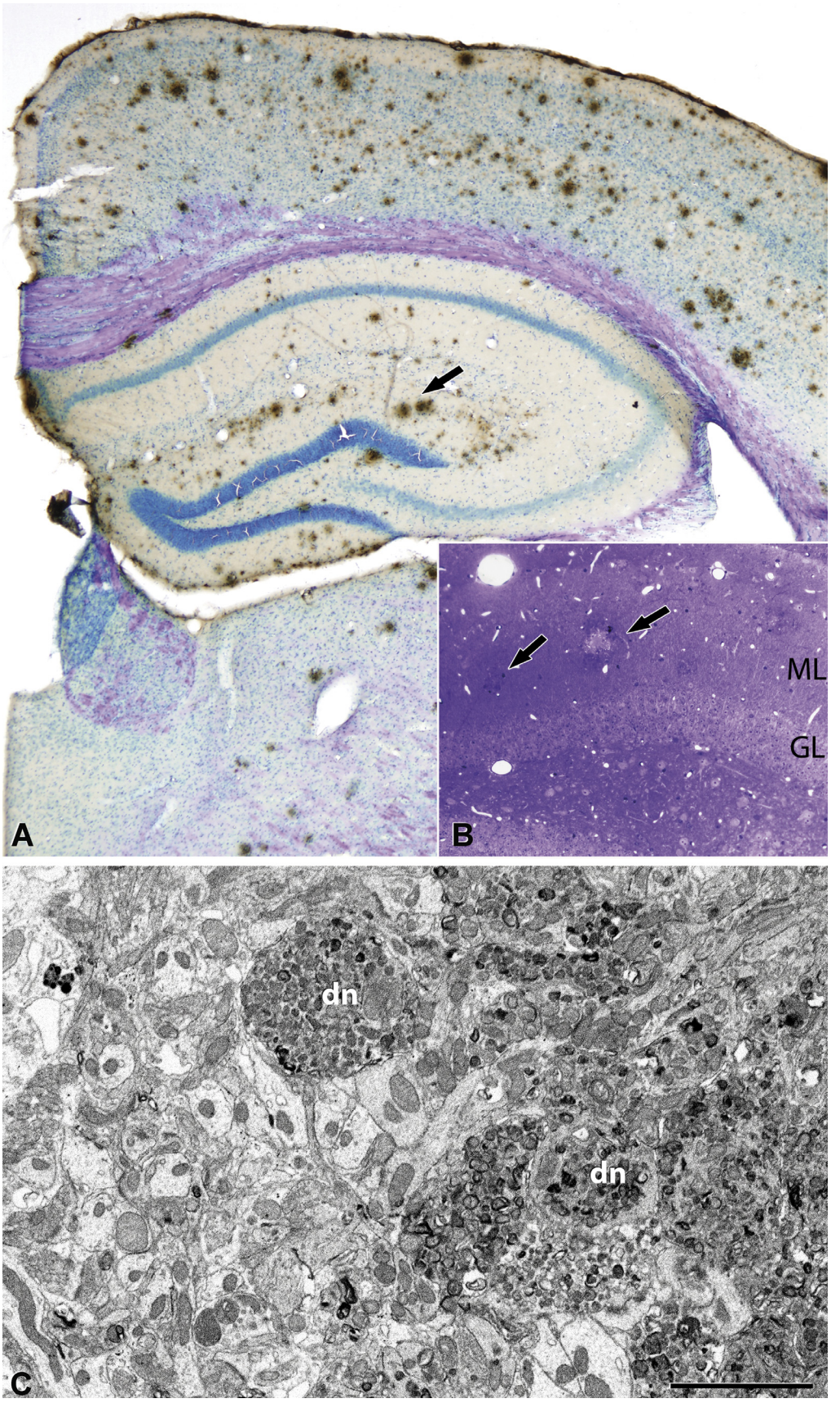

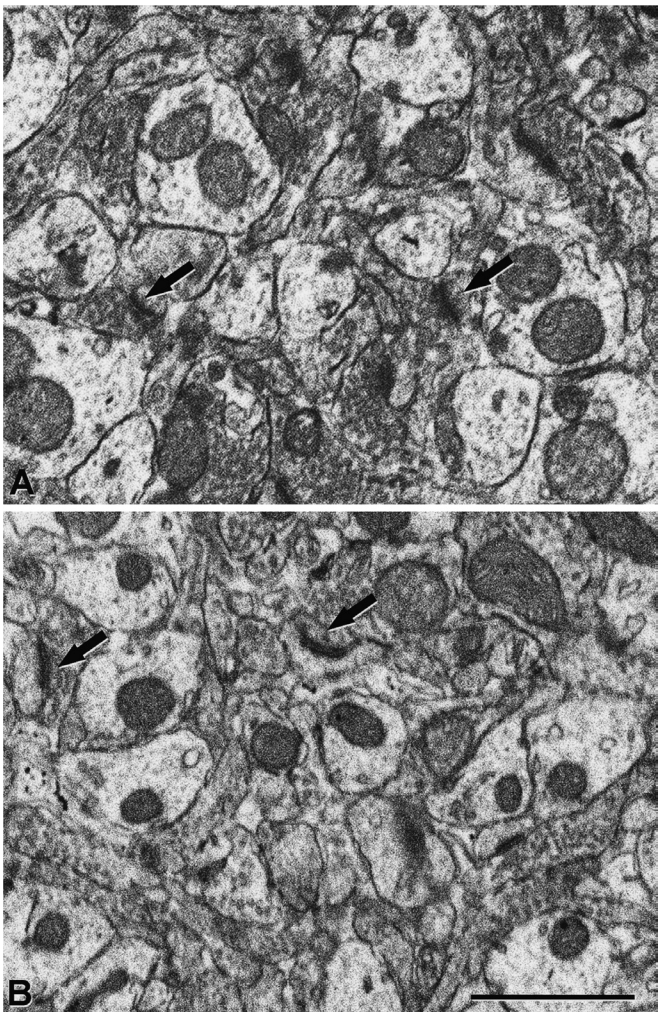

FIGURE 2. (A, B) Electron micrographs of the neuropil in the outer molecular layer from a control (TG-) **(A)** and an APP/PS1 mouse **(B)**. Arrows indicate some synapses. Scale bar in **(B)** = **(A, B)** 1 μm.

The synaptic density per unit volume (N_V) of the neuropil was calculated using the size-frequency method, which applies the formula: $N_V = N_A/d$, where N_A is the number of synaptic profiles per unit area, and d is the average cross-sectional length of synaptic junctions (15, 21). The cross-sectional length of synaptic junctions was measured using ImageJ analysis software (National Institutes of Health, Scion Corporation, Frederick, MD).

Synapse Segmentation in Stacks of FIB/SEM Images

Focused ion beam/scanning electron microscope combines a high-resolution field emission SEM column with a focused gallium ion beam, which can mill the sample surface, removing thin layers of material on a nanometer scale. After removing each 20-nm-thick slice, the milling process was paused, and the freshly exposed surface was imaged with a 2-kV acceleration potential using the in-column energy-selective backscattered electron detector. A 30-mm aperture was used, and the retarding potential of the energy-selective backscattered electron detector grid was 1,500 V. Focused ion beam/scanning electron microscope provided stacks of images of the tissue samples. The milling/imaging processes are automatically repeated to obtain long series of images that represent a 3-D sample of tissue (21). For this study, we obtained 2,048 × 1,536 pixel images at a resolution of 3.7 to 4.9 nm per pixel. The resulting stacks of images were processed as previously described (16). Briefly, image stacks were aligned (rigid registration method, translation only, no rotation), filtered (Gaussian filter), and saved using FIJI software (16). Segmentation of synapses was then performed using EspINA software. Synapse segmentation is the 3-D reconstruction of the synaptic junction. All the voxels comprising a segmented synapse are connected and are considered as a single object (Fig. 3; http://cajalbbp.cesvima.upm.es/espina). This software tool performs automated segmentation and counts synapses present in a 3-D volume of tissue. The tool allows the user to supervise the process of segmentation, reconstruction, and counting and also modifies the appropriate parameters and validates the results.

Synapses can be completely reconstructed in 3-D using EspINA (Fig. 3). Each synapse comprises the active zone (AZ), the postsynaptic density (PSD), and the synaptic cleft. At the EM level, both the AZ and the PSD appear as dark structures (25), which allows them to be segmented and reconstructed in 3-D (26). Because the AZ and the PSD are in close apposition and their areas are very similar (27), they can be represented by a single free-form surface located within the volume of the reconstructed synaptic junction. For the sake of clarity, we will refer to this surface as the ''synaptic apposition surface'' (SAS).

In addition, to quantify the number of objects (synapses) per unit volume, a 3-D counting frame (CF) was constructed within every stack (Fig. 3). This unbiased CF is a regular rectangular prism enclosed by 3 acceptance planes and 3 exclusion planes marking its boundaries (28). All objects within the CF or intersecting any of the acceptance planes are counted, whereas any object outside the CF or intersecting any of the exclusion planes is not. Because the volume of each stack of sections was known, numbers of synapses per unit volume were calculated directly by dividing the total number of synapses counted by the volume of the 3-D CF. Thus, synapses were considered as 3-D objects the contours or traces of which appeared in several consecutive sections. Special attention was paid to the fact that some of these traces could intersect one of the acceptance or exclusion planes while others might not. The intersection of a single trace with one of the acceptance

FIGURE 1. (A) Low-magnification photomicrograph of a coronal brain section from an APP/PS1 mouse immunostained with anti–β-amyloid peptide (Aβ) and counterstained with toluidine blue. Arrow indicates some Aβ plaques located in the molecular layer (ML) of the dentate gyrus (DG). **(B)** Toluidine blue–stained semithin section showing the DG and Aβ plaques (some indicated by arrows). **(C)** Electron micrograph of the neuropil adjacent to an Aβ plaque in the outer molecular layer from an APP/PS1 mouse. dn, dystrophic neurites. Scale bar (in **C**) = **(A)** 250 μm; **(B)** 50 μm; **(C)** 2.7 μm. GL, granular layer.

or exclusion planes was sufficient for the whole 3-D object to be counted. Similarly, a single trace intersecting one of the exclusion planes led to the exclusion of the whole 3-D object. Based on these criteria, EspINA produced a data table containing all the measurements extracted from every segmented synapse (SAS, volume, physical size, centroid, and Feret diameter, among other parameters) and the dimensions of the CF (Fig. 3).

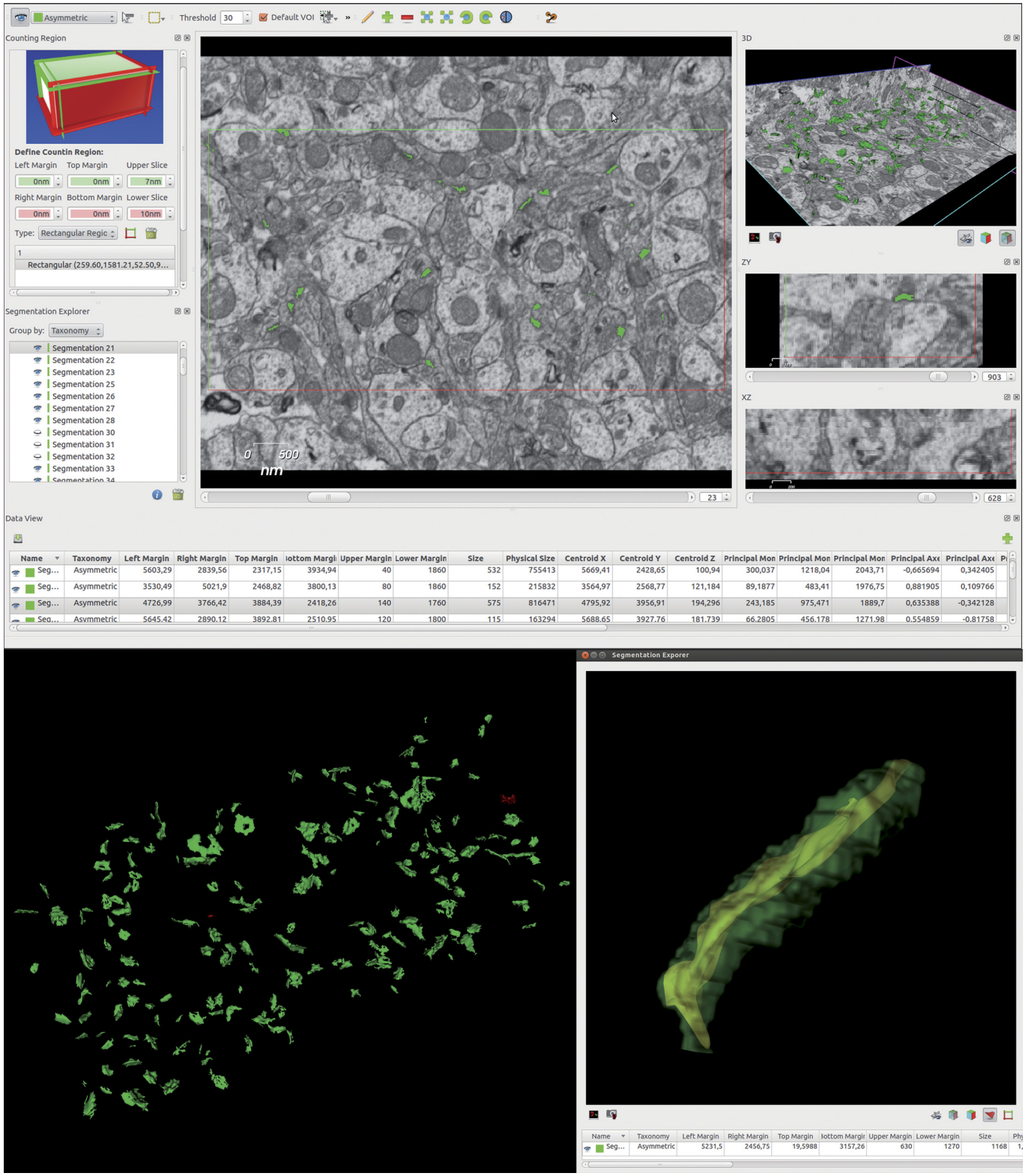

TABLE. Number of Synapses in the Focused Ion Beam/Scanning Electron Microscope Counting Frame Volume Per Sample

Mice	No. Synapses	CF Volume, μm^3	CF Volume/Mean CF, %	Calculated Synapses in a Mean CF
TG-(1)	233 (230A/3S)	48.18	46	509 (502A/7S)
TG-(2)	315 (308A/7S)	67.41	64	492 (481A/11S)
TG-(3)	469 (464A/5S)	77.67	73	644 (637A/7S)
APP/PS1 (1)	989 (958A/31S)	275.62	261	379 (367A/12S)
APP/PS1 (2)	106 (103A/3S)	32.62	31	342 (332A/10S)
APP/PS1 (3)	283 (279A/4S)	148.82	141	200 (197A/3S)
APP/PS1 (4)	267 (264A/3S)	88.04	84	319 (315A/4S)
APP/PS1 (5)	475 (465A/10S)	105.43	100	474 (464A/10S)

Representativeness of the samples calculated as a percentage, dividing the CF volume by the mean CF volume.
A, asymmetric synapses; CF, counting frame; S, symmetric synapses; TG-, control mice.

Analysis of the Spatial Distribution of the Synapses

To explore the spatial distribution pattern of synaptic junctions in the stacks of images, we used spatial statistical tools (29) (Supplemental Digital Content 1, http://links.lww.com/NEN/A443).

Statistical Analyses

Data analysis and statistical comparisons between the groups were performed using the unpaired Mann-Whitney U and 2-sample Kolmogorov-Smirnov (KS) tests for comparisons between independent samples. The 2-sample KS test uses the maximal distance between cumulative frequency distributions of these 2 samples as the statistic. The advantage of this test is that it makes no assumption about the distribution of data. In addition, it is an exact test that is independent of the sample size for the approximations (30–37). Statistical studies were performed using the GraphPad Prism statistical package (GraphPad Prism 5.0; GraphPad Software, Inc., San Diego, CA) and STATISTICA (StatSoft, Inc., Tulsa, OK).

RESULTS

In agreement with previous reports (38), immunostaining with anti-human Aβ antibody revealed the presence of numerous Aβ plaques throughout the brain (Fig. 1A).

Transmission Electron Microscopy

To analyze the ultrastructure of the neuropil in the plaque-free regions, we used a simple sampling method that consists of resectioning into ultrathin sections the same semithin sections used for determining cortical layers or regions of interest instead of obtaining ultrathin sections adjacent to these semithin sections (18). The main advantage of this method is that it allows us to study accurately the light microscope–selected neuropil regions within any given layer or region (Fig. 1B). Synapses were studied in the neuropil of the outer molecular layer (OML) in the DG of both APP/PS1 and TG- mice. Regions adjacent to the Aβ plaques showed numerous dystrophic neurites and a variety of alterations, as previously described (Fig. 1C) (39), whereas the ultrastructure of the neuropil at a distance from the external boundary of the Aβ plaques was indistinguishable in TG- mice from that of APP/PS1 mice (Fig. 2).

Estimation of Synaptic Density by the Size-Frequency Method

Synapses were quantified in the neuropil (i.e. avoiding the neuronal and glial somata and blood vessels) (15). Based on single-section studies under TEM, the synapses were classified into 3 categories according to their morphology: asymmetric, symmetric, and uncharacterized. In general, in single-section studies under TEM, a large proportion of synaptic junctions (varying between 40% and 60%) are uncharacterized (15). In this study, uncharacterized synapses were included in the final estimate of the total synaptic density. The total number of synapses in each group studied by this method was 777 in the TG- and 903 in the APP/PS1 mice.

We found significant differences in the number of total synapses per volume of the OML between TG- (mean ± SD, 31.03 ± 8.4 synapses × $10^8/mm^3$) and APP/PS1 mice (27.7 ± 8.4, $p < 0.05$ by KS test), indicating a decrease (12%) in the number of synapses per volume in the APP/PS1 animals.

Synaptic 3-D Distribution

From each of the 8 samples obtained with the FIB/SEM (3 samples from TG-, 5 from APP/PS1), we obtained the number of synapses and the inclusion volume of the 3-D counting frames (Fig. 3; Table). The total number of synapses studied by this method was 1,017 in the TG- and 2,120 in the APP/PS1 mice.

To investigate the 3-D distribution of the synapses, we first analyzed the distribution fitting of the synaptic sizes

FIGURE 3. Screenshot of the EspINA software user interface. In the main window (top), the sections are viewed through the *xy* plane, as obtained by focused ion beam/scanning electron microscope (FIB/SEM) technology. The other 2 orthogonal planes, *yz* and *xz*, are also shown in their respective windows. Using the ''Define counting region'' window, the user can choose the position of the 6 planes: the acceptance planes (green) correspond to the front, top, and left sides of the stack and the exclusion planes (red) are the back, right, and bottom sides. The ''Data view'' window shows morphometric values extracted from the reconstructed 3-dimensional (3-D) objects. The 3-D windows show the 3 orthogonal planes and the 3-D reconstruction (bottom left) of the segmented objects. Segmented objects appear in green (asymmetric synapses) or red (symmetric synapses) according to the colors selected by the user. The ''Segmentation explorer'' (bottom right) displays the synaptic apposition surface extracted from a selected object and its 3-D reconstructed volume, as well as its morphometric values.

(choosing the Feret diameter as a representative value of the size) (29). The closest fit was with a log-normal distribution according to KS 2-sided, Cramer-von Misses, and Anderson-Darling tests. Then, to study the spatial distribution of the synapses, we calculated the F, G, and K functions of each sample, comparing each with 100 simulations of the random sequential adsorption (RSA) process, with the same number of points (Supplemental Digital Content 1, Figure S1, http://links.lww.com/NEN/A443). The KS 2-sided test was used to test the similarity between the samples and RSA simulations (Supplemental Digital Content 1, Table S1, http://links.lww.com/NEN/A443). Results obtained in these comparisons indicated a clear fit of the samples to an RSA ($p > 0.95$). Thus, we can conclude that the spatial organization of synapses in the neuropil of the OML is random, regardless of the type of sample (APP/PS or TG-).

Direct Quantification of Synapses From Stacks of Serial Sections

In the FIB/SEM samples, numbers of synapses per unit volume were calculated directly by dividing the total number of synapses counted by the volume of the CF. The estimation of the representativeness of each sample allowed us to compare the number of synapses per volume between samples. We first calculated the mean of the CF volume of all samples (mean CF, 0.105 μm^3). We then estimated the representativeness of each sample as a percentage, which was calculated by dividing its CF volume by the mean CF (Table). Then, assuming that all samples were comparable, the number of synapses was recalculated (Table). These estimates were possible because the random spatial distribution of synapses had been previously demonstrated in all the samples.

Because all the samples were considered to be representative, it was possible to compare the synaptic density between the TG- and APP/PS1 groups and to conclude that the number of synapses per volume in APP/PS1 (mean ± SD, 32.6 ± 9.5 synapses × $10^8/mm^3$) was significantly lower (~37% less) than that in TG- mice (52.2 ± 7.9; $p < 0.0001$ by KS test). These results were consistent with the previous estimation of the synaptic densities performed with TEM samples using the size-frequency method.

Identification of the Postsynaptic Elements

Because a lower value in the synaptic density per volume was found in the neuropil from APP/PS1 mice, we investigated if these changes were specific to any postsynaptic target. For this purpose, we identified the different postsynaptic elements in FIB/SEM images stacks. To this end, a representative sample of synapses was chosen for examination. According to a simple sampling of the total population of synapses (40), we selected a total of 94 synapses (46 from TG-; 48 from APP/PS1) based on the maximum error of 0.1 and the confidence level of 0.95 (Supplemental Digital Content 1, Equation F, http://links.lww.com/NEN/A443). We observed that, in TG- samples, 89.11% of the synapses were on dendritic spines and 10.89% were on dendritic shafts. Similarly, in APP/PS1 samples, 91.65% of the synapses were located on dendritic spines and 8.35% on dendritic shafts. Since the maximum error of the sampling was 10%, no significant differences were found in the proportion of the type of postsynaptic elements between TG- and APP/PS1.

Volumetric Characteristics of Synapses

For the detailed analysis of their morphology, synapses were sampled and analyzed using an algorithm capable of extracting the SAS from a 3-D volume representing a previously segmented synaptic junction (26). The SAS is equivalent to the AZ and the PSD, the 2 major components of the presynaptic and postsynaptic membranes. Thus, the algorithm provides crucial morphologic information that enables the functional characteristics of synapses to be correlated with their geometric properties.

In the present study, a total of 3,071 asymmetric synapses located in the neuropil of the OML from the DG were fully reconstructed (n = 1,002 from TG- mice; n = 2,069 from APP/PS1 mice). Values of SAS were fitted to a log-normal distribution in both groups. The average SAS area was 41% larger in APP/PS1 (mean ± SEM, 46,130 ± 707 nm^2) than in TG- mice (32,700 ± 688 nm^2; $p < 0.05$ by Mann-Whitney U

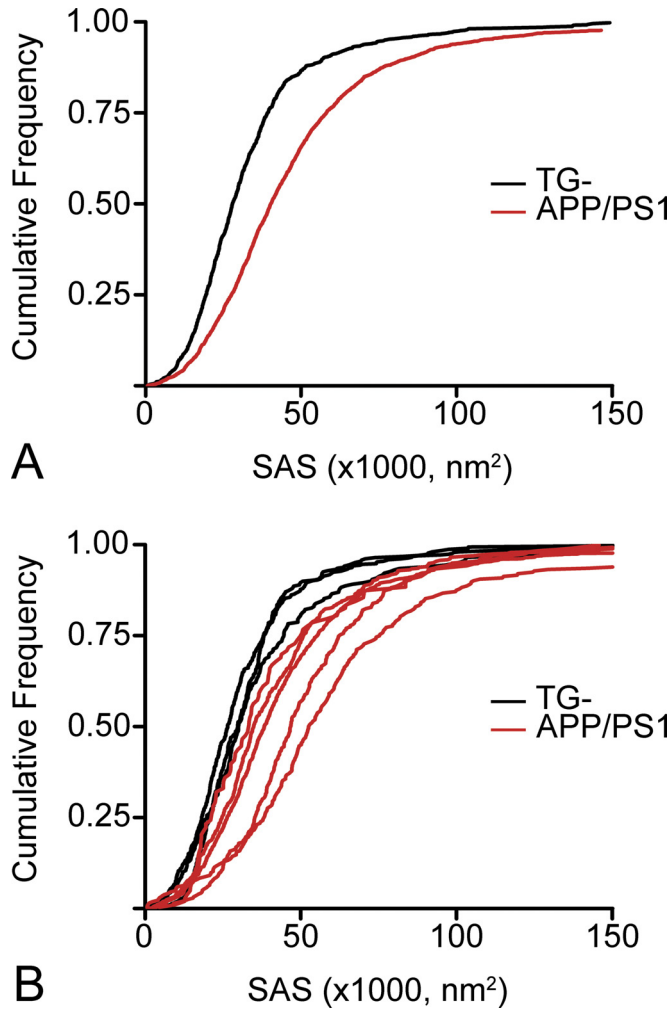

FIGURE 4. Cumulative frequency plots showing the value distribution of the synaptic apposition surface (SAS). **(A, B)** Comparisons per group **(A)** and per sample **(B)** show higher SAS values in APP/PS1 compared with control (TG-) mice.

test and $p < 0.0001$ by KS test). Moreover, frequency analysis revealed that the within-group distribution was also significantly different ($p < 0.0001$ by KS test) between groups (Fig. 4). In the APP/PS1, there was a 20% increase in the prevalence of large synapses (SAS, >50,000 nm^2); whereas in the TG- mice, there was a 26% higher proportion of medium-size synapses (SAS, <30,000 nm^2). Our results indicate that large synapses represent 35% of the APP/PS1 synapses but only 14% of the TG- synapses.

DISCUSSION

In the present study, the ultrastructural analysis of the OML neuropil shows that the total number of synapses per volume in the plaque-free areas of APP/PS1 mice was lower than that in TG- mice. Moreover, in the APP/PS1 mice, larger synapses were more frequent than that in TG- mice, indicating significant changes in both the number and morphology of the synapses.

The OML of the DG receives neuronal fibers arising from layer II of the entorhinal cortex and granular neurons of the DG project to CA3, which is a part of the corticohippocampal circuit associated with memory (41–44). Therefore, synaptic changes in this circuit most likely affect the normal mnesic process. Because hippocampal-dependent cognitive impairment has been observed in APP/PS1 mice (14), the synaptic changes found in the OML may represent a microanatomic substrate of the altered cognitive function observed in this model.

Decrease in the Synaptic Density

The present results are consistent with previous studies performed in the brains of AD patients that indicated that synapse loss occurs in the DG (6, 8, 45, 46). On the other hand, other studies on synaptic densities in the DG from Tg2576 transgenic mice have reported an increase (47), a decrease (48), or no alterations in synaptic density as in APP/PS1 mice (49) versus nontransgenic animals. Differences in estimates of synapse densities might be attributable to the diversity of transgenic mouse models examined. In addition, some studies performed in AD mouse models have quantified synapses by immunostaining of synaptic proteins such as synaptophysin (48, 50–53), and discrepancies have been found between different methodologies. For example, it has been reported no changes in synaptophysin expression but a significant decrease in synaptic density analyzed by TEM in the OML of the DG in a transgenic mouse model of AD (48). The discrepancy between estimation of synapses by immunostaining and TEM can be explained by the fact that counting of immunoreactive puncta at the light microscope level is clearly less accurate than the estimation of synapses identified at the EM level. In addition, synaptophysin immunostaining labels a specific protein of the presynaptic terminal, but it does not necessarily mean that they establish a synaptic junction. Thus, EM is the method of choice to estimate changes in synaptic density.

Comparison With Previous Light Microscopy Studies on Dendritic Spines

In the present study, using both TEM and FIB/SEM, we found a significant loss of synapses per unit volume in the OML of the APP/PS1 mice in the same area where we previously found no changes in dendritic spine density (13). In addition, here we observed that the decrease of synapses was caused by a loss of synapses in both the dendritic spines and dendritic shafts. It is widely assumed that each dendritic spine in the cerebral cortex establishes a synapse. However, there are nonsynaptic spines (54), and, although they represent a small percentage in the cerebral cortex (~4%), a possible explanation for this discrepancy between the findings of no changes in number of dendritic spines but lower density of synapses could be an increase in the number of nonsynaptic dendritic spines.

In AD, there is a degeneration of the synapses caused by toxic effects of Aβ oligomers (55). Association of Aβ oligomers with synaptic structures has been related to alterations in both synapses and dendritic spines (55–57). Moreover, it has been reported that before synapse loss, Aβ oligomers induce profound changes in the composition of synaptic membranes (57). Thus, it is likely that, in the OML from APP/PS1 mice, a moderate number of synaptic dendritic spines may have alterations in their protein machinery caused by Aβ oligomers, and that these dendritic spines would then turn into nonsynaptic dendritic spines.

Alterations in Synaptic Morphology

The geometry and morphologic characteristics of the synaptic junction provide useful information of synaptic function. At the presynaptic membrane, the AZ contains the molecular machinery necessary for the rapid docking of synaptic vesicles and zthe subsequent release of neurotransmitters (58, 59). It has been shown that the surface area of the AZ is proportional to the probability of vesicle release (60), whereas the area of the PSD is proportional to the number of postsynaptic receptors (61). Thus, a higher proportion of large synapses in the neuropil of the OML from APP/PS1 mice would imply enlarged AZ and/or PSD in those synapses, which would involve an increased synaptic transmission.

However, in the plaque-free regions of the OML in the DG from APP/PS1 mice, a decrease of 38% in the prevalence of large spines (whose head volume was >0.1 μm^3) has been previously described (13). The apparent discrepancy between these results and the present findings regarding synaptic size can be explained by specific morphologic changes in the postsynaptic element. That is, large dendritic spines may reduce their cytoplasm volume and simultaneously remake their postsynaptic element induced by Aβ oligomers, increasing the size of the AZ and/or PSD. Thus, in the neuropil of APP/PS1 mice, there would be dendritic spines with reduced head size containing larger synaptic junctions. Changes in the size of the AZ and/or PSD have been reported under a variety of normal and experimental conditions and, in general, these changes have been associated with plastic responses (60, 62). The increased synaptic size found in the present study may, therefore, represent a mechanism of functional compensation for the general synaptic loss in the neuropil but also might denote a synaptic alteration or malfunction. Further experiments would be necessary to determine the physiologic consequences of these changes in this particular hippocampal region of APP/PSS1 mice.

Finally, it should be noted that caution is needed regarding extrapolation of the present results to interpret changes in AD patients not only because of the differences in brain organization between humans and mice (63) but also because the mouse model used in the present study does not develop other typical pathologic alterations observed in AD patients such as neurofibrillary changes (38). However, this mouse model is useful for isolating effects of Aβ overproduction and deposition on brain circuitry and for distinguishing them from other changes in dendritic spines that may be induced by the presence of hyperphosphorylation of tau in neurons.

ACKNOWLEDGMENTS

The authors thank the computer resources, technical expertise, and assistance provided the Centro de Supercomputación y Visualización de Madrid. Lidia Alonso-Nanclares thanks all laboratory members for their comments to improve this work and J. Morales, J. Peña, and F. de las Pozas for their contributions to EspINA software.

REFERENCES

1. Jucker M, Beyreuther K, Haass C, et al. *Alzheimer: 100 Years and Beyond*. Berlin/Heidelberg, Germany: Springer-Verlag, 2006
2. Nelson PT, Alafuzoff I, Bigio EH, et al. Correlation of Alzheimer disease neuropathologic changes with cognitive status: A review of the literature. J Neuropathol Exp Neurol 2012;71:362–81
3. Masliah E, Terry RD, DeTeresa RM, et al. Immunohistochemical quantification of the synapse-related protein synaptophysin in Alzheimer disease. Neurosci Lett 1989;103:234–39
4. Terry RD, Masliah E, Salmon DP, et al. Physical basis of cognitive alterations in Alzheimer's disease: Synapse loss is the major correlate of cognitive impairment. Ann Neurol 1991;30:572–80
5. DeKosky ST, Scheff SW, Styren SD. Structural correlates of cognition in dementia: Quantification and assessment of synapse change. Neurodegeneration 1996;5:417–21
6. Scheff SW, Price DA. Synaptic density in the inner molecular layer of the hippocampal dentate gyrus in Alzheimer disease. J Neuropathol Exp Neurol 1998;57:1146–53
7. Coleman PD, Yao PJ. Synaptic slaughter in Alzheimer's disease. Neurobiol Aging 2003;24:1023–27
8. Scheff SW, Price DA. Alzheimer's disease–related alterations in synaptic density: Neocortex and hippocampus. J Alzheimers Dis 2006;9:101–15
9. Perl DP. Neuropathology of Alzheimer's disease. Mt Sinai J Med 2010; 77:32–42
10. Spires-Jones T, Knafo S. Spines, plasticity, and cognition in Alzheimer's model mice. Neural Plast 2012;2012:319836
11. Andersen P. *The Hippocampus Book*. New York, NY: Oxford University Press, 2007
12. Li B, Yamamori H, Tatebayashi Y, et al. Failure of neuronal maturation in Alzheimer disease dentate gyrus. J Neuropathol Exp Neurol 2008; 67:78–84
13. Knafo S, Alonso-Nanclares L, Gonzalez-Soriano J, et al. Widespread changes in dendritic spines in a model of Alzheimer's disease. Cereb Cortex 2009;19:586–92
14. Malm TM, Iivonen H, Goldsteins G, et al. Pyrrolidine dithiocarbamate activates Akt and improves spatial learning in APP/PS1 mice without affecting beta-amyloid burden. J Neurosci 2007;27:3712–21
15. DeFelipe J, Marco P, Busturia I, et al. Estimation of the number of synapses in the cerebral cortex: Methodological considerations. Cereb Cortex1999;9:722–32
16. Morales J, Alonso-Nanclares L, Rodriguez JR, et al. Espina: A tool for the automated segmentation and counting of synapses in large stacks of electron microscopy images. Front Neuroanat 2011;5:18
17. Scheuner D, Eckman C, Jensen M, et al. Secreted amyloid beta-protein similar to that in the senile plaques of Alzheimer's disease is increased in vivo by the presenilin 1 and 2 and APP mutations linked to familial Alzheimer's disease. Nat Med 1996;2:864–70
18. DeFelipe J, Fairén A. A simple and reliable method for correlative light and electron microscopic studies. J Histochem Cytochem 1993;41: 769–72
19. Peachey LD. Thin sections. I. A study of section thickness and physical distortion produced during microtomy. J Biophys Biochem Cytol 1958;4: 233–42
20. Alonso-Nanclares L, Gonzalez-Soriano J, Rodriguez JR, et al. Gender differences in human cortical synaptic density. Proc Natl Acad Sci USA 2008;105:14615–19
21. Merchán-Pérez A, Rodriguez JR, Alonso-Nanclares L, et al. Counting synapses using FIB/SEM microscopy: A true revolution for ultrastructural volume reconstruction. Front Neuroanat 2009;3:18
22. Gray EG. Electron microscopy of synaptic contacts on dendrite spines of the cerebral cortex. Nature 1959;183:1592–93
23. Colonnier M. Synaptic patterns on different cell types in the different laminae of the cat visual cortex. An electron microscope study. Brain Res 1968;9:268–87
24. Peters A, Palay SL, Webster HD. *The Fine Structure of the Nervous System. Neurons and Their Supporting Cells*. New York, NY: Oxford University Press, 1991
25. Peters A, Palay SL. The morphology of synapses. J Neurocytol 1996;25: 687–700
26. Morales J, Rodriguez A, Rodriguez J-R, et al. Characterizing and extracting the synaptic apposition surface for the analysis of synaptic geometry. In: Peña JM, Famili F, eds. *5th Workshop on Data Mining in Functional Genomics and Proteomics: current trends and future directions*. Madrid, GMRV Publications, 2011:63–72
27. Schikorski T, Stevens CF. Quantitative ultrastructural analysis of hippocampal excitatory synapses. J Neurosci 1997;17:5858–67
28. Howard CV, Reed MG. *Unbiased Stereology: Three-Dimensional Measurement in Microscopy*. 2nd Ed. Oxon, UK: Garland Science/BIOS Scientific Publishers, 2005
29. Merchán-Pérez A, Rodriguez JR, Gonzalez S, et al. Three-dimensional spatial distribution of synapses in the neocortex: A dual-beam electron microscopy study. Cereb Cortex 2013 Jan 30. [Epub ahead of print] PMID: 23365213.
30. Siegel S. Nonparametric statistics. American Statistician 1957;11:13–19
31. Scholz FW, Stephens MA. K-sample Anderson-Darling tests. J Am Stat Assoc 1987;82:918–24
32. Motulsky H. *Intuitive Biostatistics*. New York, NY: Oxford University Press, 1995
33. Conover WJ. *Practical Nonparametric Statistics*. 3rd Ed. New York, NY: John Wiley and Sons, 1999
34. Hollander M, Wolfe DA. *Nonparametric Statistical Methods*. 2nd Ed. New York, NY: John Wiley & Sons, 1999
35. NIST. *e-Handbook of Statistical Methods*. NIST/SEMATECH, 2003
36. Ricci V. Rappresentazione analitica delle distribuzioni statistiche con R. Economia e Commercio 2005;1/2:47–60
37. Corder GW, Foreman DI. *Nonparametric Statistics for Non-Statisticians: A Step-by-Step Approach*. Hoboken, NJ: John Wiley & Sons, 2009
38. Irizarry MC, McNamara M, Fedorchak K, et al. APPSw transgenic mice develop age-related A beta deposits and neuropil abnormalities, but no neuronal loss in CA1. J Neuropathol Exp Neurol 1997;56:965–73
39. Garcia-Marin V, Blazquez-Llorca L, Rodriguez JR, et al. Diminished perisomatic GABAergic terminals on cortical neurons adjacent to amyloid plaques. Front Neuroanat 2009;3:28
40. Osuna JR. *Métodos de muestreo. Casos prácticos*. Madrid, Spain: Centro de Investigaciones Sociológicas, 2005
41. Witter MP, Amaral DG. Hippocampal formation. In: Paxinos G, ed. *The Rat Nervous System*. San Diego, CA: Elsevier Academic Press, 2004: 635–704
42. Kesner RP, Lee I, Gilbert P. A behavioral assessment of hippocampal function based on a subregional analysis. Rev Neurosci 2004;15:333–51
43. Buhl E, Whittington M. Local circuits. In: Andersen PM, Amaral R, DT Bliss DT, O'Keefe J, eds. *The Hippocampus Book*. New York, NY: Oxford University Press, 2007:297–320
44. Spruston N, McBain C. Structural and functional properties of hippocampal neurons. In: Andersen PM, Amaral R, DT Bliss DT, O'Keefe J, eds. *The Hippocampus Book*. New York, NY: Oxford University Press, 2007:133–202

45. Scheff SW, Sparks DL, Price DA. Quantitative assessment of synaptic density in the outer molecular layer of the hippocampal dentate gyrus in Alzheimer's disease. Dementia 1996;7:226–32
46. Masliah E, Crews L, Hansen L. Synaptic remodeling during aging and in Alzheimer's disease. J Alzheimers Dis 2006;9:91–99
47. King DL, Arendash GW. Maintained synaptophysin immunoreactivity in Tg2576 transgenic mice during aging: Correlations with cognitive impairment. Brain Res 2002;926:58–68
48. Dong H, Martin MV, Chambers S, et al. Spatial relationship between synapse loss and beta-amyloid deposition in Tg2576 mice. J Comp Neurol 2007;500:311–21
49. Malthankar-Phatak GH, Lin YG, Giovannone N, et al. Amyloid deposition and advanced age fails to induce Alzheimer's type progression in a double knock-in mouse model. Aging Dis 2012;3:141–55
50. Dodart JC, Mathis C, Saura J, et al. Neuroanatomical abnormalities in behaviorally characterized APP(V717F) transgenic mice. Neurobiol Dis 2000;7:71–85
51. Boncristiano S, Calhoun ME, Howard V, et al. Neocortical synaptic bouton number is maintained despite robust amyloid deposition in APP23 transgenic mice. Neurobiol Aging 2005;26:607–13
52. Rutten BP, Van der Kolk NM, Schafer S, et al. Age-related loss of synaptophysin immunoreactive presynaptic boutons within the hippocampus of APP751SL, PS1M146L, and APP751SL/PS1M146L transgenic mice. Am J Pathol 2005;167:161–73
53. Noristani HN, Meadows RS, Olabarria M, et al. Increased hippocampal CA1 density of serotonergic terminals in a triple transgenic mouse model of Alzheimer's disease: An ultrastructural study. Cell Death Dis 2011;2:e210
54. Arellano JI, Espinosa A, Fairen A, et al. Nonsynaptic dendritic spines in neocortex. Neuroscience 2007;145:464–69
55. Wilcox KC, Lacor PN, Pitt J, et al. Abeta oligomer-induced synapse degeneration in Alzheimer's disease. Cell Mol Neurobiol 2011;31:939–48
56. Gylys KH, Fein JA, Yang F, et al. Synaptic changes in Alzheimer's disease: Increased amyloid-beta and gliosis in surviving terminals is accompanied by decreased PSD-95 fluorescence. Am J Pathol 2004;165:1809–17
57. Lacor PN, Buniel MC, Furlow PW, et al. Abeta oligomer-induced aberrations in synapse composition, shape, and density provide a molecular basis for loss of connectivity in Alzheimer's disease. J Neurosci 2007;27:796–807
58. Owald D, Sigrist SJ. Assembling the presynaptic active zone. Curr Opin Neurobiol 2009;19:311–18
59. Sigrist SJ, Schmitz D. Structural and functional plasticity of the cytoplasmic active zone. Curr Opin Neurobiol 2011;21:144–50
60. Matz J, Gilyan A, Kolar A, et al. Rapid structural alterations of the active zone lead to sustained changes in neurotransmitter release. Proc Natl Acad Sci USA 2010;107:8836–41
61. Nusser Z, Hajos N, Somogyi P, et al. Increased number of synaptic GABA(A) receptors underlies potentiation at hippocampal inhibitory synapses. Nature 1998;395:172–77
62. Desmond NL, Levy WB. Changes in the postsynaptic density with long-term potentiation in the dentate gyrus. J Comp Neurol 1986;253:476–82
63. DeFelipe J. From the connectome to the synaptome: An epic love story. Science 2010;330:1198–201

